Structure and dynamics of small polyimide oligomers with silicon as a function of aging

Structure and dynamics of small polyimide oligomers with silicon as a function of aging

Mary K. Burdette-Trofimov*,†, Beth L. Armstrong*,‡, Luke Heroux¶, Mathieu Doucet¶, Robert L. Sacci†, and Gabriel M. Veith*,†

†Chemical Sciences Division, Oak Ridge National Laboratory

‡ Materials Science and Technology Division, Oak Ridge National Laboratory

¶Neutron Scattering Division, Oak Ridge National Laboratory

E-mail: burdettekk@ornl.gov, armstrongbl@ornl.gov, veithgm@ornl.gov

ORCID
Mary K. Burdette-Trofimov: https://orcid.org/0000-0003-2395-2867
Beth L. Armstrong: https://orcid.org/0000-0001-7149-3576
Luke Heroux: https://orcid.org/0000-0001-8993-3904
Mathieu Doucet: https://orcid.org/0000-0002-5560-6478
Robert L. Sacci: https://orcid.org/0000-0002-0073-5221
Gabriel M. Veith: https://orcid.org/0000-0002-5186-4461

Abstract

The effect of UV curing and shearing on the structure and behavior of a polyimide (PI) binder as it disperses silicon particles in a battery electrode slurry was investigated. PI dispersant effectiveness increases with UV curing time which controls the overall binder molecular weight. The shear during electrode casting causes higher molecular weight PI to agglomerate resulting in battery anodes with poorly dispersed Si particles that do not cycle well. It is hypothesized that when PI binder is added above a critical amount it conformally coats the silicon particles and greatly impedes Li ion transport. There is an "interzonal region" for PI binder loading where it disperses silicon well and provides a coverage that facilitates Li transport through the anode material and into the silicon particles. These results have implications in ensuring reproducible electrode manufacturing and increasing cell performance by optimizing the PI structure and coordination with the silicon precursor.

Introduction

Polyimides (PI) is a candidate for multi-functional binders in composite silicon anodes due to their mechanical robustness (Young's modulus ~14.5 GPa and tensile strength 7.5 GPa) and lithium ion and electronic conductivity.[1-2] There are many different PI-based binders,[1, 3-7] from fully cured aromatic polyimide binders that require no post-thermal treatment after electrode fabrication[5, 8-9] to uncured precursor monomers/oligomers that need a UV/thermal curing post-processing step. [2, 4] Fully cured aromatic polyimide binders (e.g., P84 by Evonik and Ensinger) bind silicon through hydrogen bonding with interfacial Si-H and Si-H-N moities.[5] Uncured PI precursor formulations (e.g., Dreambond100 binder by IST Corporation) are typically made of poly(amic acids), which require heating between 170-370°C to produce the C-O-C crosslinks (~180 °C) and the ring closing condensation reaction (~350 °C).[2, 4, 6-7] This *in situ* polymerization step forms silyl benzoates and additional C-O-C crosslinks that bind the silicon particles.[4]

How PI precursor solution aging affects electrode casting slurry dynamics and the resulting architecture is not well explored. Poly(amic acids) and their derivatives are easily susceptible to UV curing and cross-linking[10-13], which occurs during long-term storage. Many battery researchers make large quantities of binder stock solution for use in casting multiple electrodes over an extended period of time (on the order of months). However, making a stock solution of a binder may result in electrode slurries that contain an unknown and uncontrolled distribution of polyimide chains and molecular weights. It was previously shown that poly(acrylic acid) (PAA) and lithiated PAA (LiPAA) molecular weight plays a critical role in slurry dynamics, electrode morphology and homogeneity, and electrochemical performance.[14] Therefore, PI precursor aging could inadvertently result in slurries and electrodes with vastly

different mechanical and electrochemical properties that are more correlated to *when* the slurry was made and less so to *how* it was made.

PI binder aging affects slurry and electrode homogeneity, aggregation, and agglomeration and their effect on electrochemical properties is investigated. PI monomers were UV cured at various times where crosslinking and resulting slurry dynamics were probed via infrared spectroscopy, rheology coupled ultra-small neutron scattering (rheo-USANS), and electrochemistry. It was found that PI monomers are effective dispersants at all UV cure times; however, that effect is lost with increasing shear rate (i.e., electrode casting speed). Comparison between silicon anodes fabricated with PI, PAA, and LiPAA binders suggest that too much binder coverage of the silicon does not necessarily lead to better electrochemical properties; rather, the slurry and electrode architectures are critical for improved electrochemical performance.

Experimental

Reagents and Solvents

All reagents were used without further purification unless otherwise stated. The polyimide (PI) binder, Dreambond100, was obtained from I.S.T. Corporation and was received as a 60 wt% PI solution in N-methyl-2-pyrrolidone (NMP). The exact chemical structure of the Dreambond100 is proprietary, but it is known that it is made of imide-based monomers/oligomers that have to be cured, usually thermally, to create the polyimide polymer chains. Silicon nanopowders were obtained from the Argonne National Laboratory (ANL) Cell Analysis, Modeling, and Prototyping (CAMP) Facility and used in anode A-A018 in the reference library. C-NERGY Super C45 conductive carbon black was purchased from Timcal.

Deuterated dimethylformamide (DMF) was used as a solvent due to the similar polarity and functionality as NMP, and availability in quantities required for this work. DMF was chosen as it is similar to NMP in terms of functionality and polarity. Deuterated DMF-D7 (D, 99.5%) was purchased from Cambridge Isotope Laboratories, Inc. (Tewksbury, MA). DMF for electrode fabrication was purchased from Sigma Aldrich (ACS reagent, $\geq$ 99.8%).

Slurry Preparation Method

Approximately 10 g of 60 wt% PI solution was placed in an aluminum weight boat (area of exposure: 2043 mm^2) and was cured continuously for either 10 min, 30 min, or 60 min using a Dymax Ultraviolet Light Source 5000-EC. The Dymax is a broadband UV curing oven with a spectral range from 310-390 nm. The peak of the UV light occurs at approximately 365 nm. PI binder solutions (14wt%) of various cure levels were used to make binder solutions in DMF-D7 for rheo-USANS measurements. To prepare the PI binder 14 wt% solutions, PI (uncured, 10 min UV cured, 30 min UV cured, or 60 min UV cured) was placed in DMF-D7 (~25 mL) and was mixed using a Thinky brand planetary centrifugal mixer (PCM) at 2000 rpm for two-2 min intervals. Each Thinky brand mixing jar was equipped with 5 pieces of 5 mm spherical yttria (8 mol %) stabilized zirconia (8YZ) media. After rheo-USANS was measured on the pure binder solutions, silicon (~12 g) was poured directly into the binder solution and mixed by stirring the silicon into the binder solution until the silicon was fully wetted. A rheo-USANS measurement of the binder took 24 hours, so the binder "aged" for 24 hours prior to the addition of silicon. The Si+binder slurry was pre-sheared at 5 Hz for 30 sec before rheo-USANS was performed to aid in mixing.

To prepared silicon slurries for electrochemical analysis, the slurry was made in the following order and mixed with the PCM: 1) DMF (11 g) and silicon (10 g) were mixed at

2000 rpm for 2-two minute intervals, 2) Timcal C-45 carbon black (0.59 g) was added to the

slurry and mixed at 2000 rpm for 2-two minute intervals, and 3) uncured PI 60 wt% binder

solution (1.96 g) was added to the slurry and mixed at 2000 rpm for 2-two minute intervals.

The process was repeated for the 10 min cure, 30 min cure, and 60 min cure PI 60 wt%

solution with 5 pieces of 5 mm 8YZ media.

Electrochemical Testing

A doctor blade with a 1 mil gap (25 μm) was used to cast the slurry onto battery

grade copper foil in a uniform film. The average shear rate was 610 Hz (s^{-1}) as calculated

using the simple shear rate equation.[15] Immediately after casting, the electrodes were dried in

air on a hot plate at 130°C. After air drying, electrode disks (13 mm) were punched from the

bulk electrode with a high precision electrode cutter (EL-Cut from EL-Cell). Electrode disks

were dried at 120°C under reduced pressure (27 inches Hg or 91 kPa) for 18 hours and were

transferred to the argon glove box while hot to minimize moisture contamination. The active

loading of silicon was approximately 0.5 mg/cm^2. Weight loadings were 85 wt% silicon, 5

wt% Timcal C45 carbon black, and 10 wt% PI binder. The electrodes were not calendared

after casting. Coin cells (2032 type – Pred Materials, NY) were assembled in the following

order: coin cell cap, gasket, wave washer, spacer with lithium metal adhered, one 18 mm

disk of Dreamweaver Gold separator, electrolyte, silicon anode, coin cell bottom in an argon

filled glove box. The electrolyte used was a 1.2 M lithium hexafluorophosphate solution in

battery grade ethylene carbonate and ethyl methyl carbonate (50/50 (v/v)) (Aldrich – UBE

Chemical). The electrolyte (100 μL) was placed on the Dreamweaver Gold separator. Each

half cell was cycled at a C-rate of C/5 between 1 V and 50 mV using a MACCOR battery

test stand at 30°C. Prior to discharge, the half-cell rested for 40 minutes. Between the

discharge and charge step, the half-cell rested for 10 minutes.

Materials Characterization

Rheology

Standard rheology measurements on uncured, 10 min, 30 min, and 60 min UV cured

PI binder solutions (60 wt%) and DMF based silicon electrode slurries were obtained using a

TA Instruments ARG2 rheometer equipped with the steel cup (30 mm) and bob (28 mm) cell

geometry. Each rheology measurement consisted of a pre-shear step of 5 Hz for 30 seconds

followed by a shear sweep step from 5 Hz to 1000 Hz with each viscosity point being the

average viscosity over a 30 sec time interval. All measurements were obtained at 25°C with

Peltier temperature control.

Infrared Spectroscopy

Infrared spectra were acquired in attenuated total reflection (ATR) mode on a Bruker

Inventio FTIR spectrometer. The ATR accessory (Golden Gate, Specac) used a Ge wedge crystal

with incidence and reflected light angled at 45 degree from surface normal. The sample was

pressed into the Ge surface using the supplied torque press to improve uniform surface coverage.

Mirror speed was 10 kHz, the number of integrated scans for the background and sample were

set to 128 and the resolution was 4 cm^{-1}.

Gel Permeation Chromatography

Gel permeation chromatography (GPC) was performed on the uncured, 10, 30, and 60

min UV cured PI to determine the molecular weight as a function of aging/UV curing. GPC was

performed with an Agilent 1100 series Autosampler (1313A), quaternary pump, and vacuum

degasser. The GPC columns were heated to 35°C using a Waters Temperature Control Module II and column oven. Molecular weight was detected using a flow-cell refractive index detector (ERC RefractoMax520) that was heated to 35°C. The column used was a Jordi polystyrene mixed bed column with a molecular range of 500 g/mol to 2 million g/mol, and a Jordi guard column.

All PI based polymers were dissolved in HPLC grade NMP (Sigma Aldrich) at a concentration of 5 mg/mL. Each solution was filtered through a 0.2 μm PTFE filter prior to injection. Injection volume was 40 μL with an eluent of HPLC grade NMP. Flow rate was 0.75 mL/min. Chromatograms were analyzed with Agilent ChemStation software.

Zeta Potential

Zeta potential measurements were collected using a Brookhaven ZetaPALS instrument. Samples were prepared by making a stock solution of 0.0582 g of silicon nanopowder (either as a pure powder or as a component of other slurries) in 5 mL of NMP (stock solution 1). Stock solution 1 (40 μL) was diluted into 20 mL of NMP. Immediately after dilution, the zeta potential was obtained. Measurements were obtained of the same solution 24 hours after the initial measurement. Each zeta potential measurement was the average of 10 cycles.

Refractive Index Determination

Refractive index measurements were obtained on a Mettler Toledo RM40 Refractometer. A series of dilute (0.25 wt% to 10 wt%) solutions of uncured PI or 60 min UV cured PI in NMP were measured using the refractometer to make a calibration curve of refractive index as a function of PI mass in solution. Then a series of slurries containing silicon (2 g) and 0.25 wt% to 10 wt% of uncured or 60 min UV cured PI in NMP were made. These slurries were gently

shaken using a shaker table for 3 days in the dark to ensure that the PI had ample time to adsorb onto the silicon. After 3 days, the silicon slurries were centrifuged at 6000 rpm for 30 min and the supernatant was removed. The refractive index of the supernatant was measured and correlated with the mass of PI adsorbed onto the silicon.

Neutron Scattering

Neutron studies were performed at the Spallation Neutron Source (SNS) at ORNL. USANS was used to characterize the conformation and aggregation behavior of the silicon/binder slurries as a function of binder preparation method over a wide range of length scales, from approximately 200 nm to approximately 10 μm. For all neutron measurements, the scattering intensity is measured as a function of the wave-vector transfer Q is described by Equation 1 where λ is the neutron wavelength and θ is the scattering angle.[16] The USANS instrument used in this investigation is a time-of- flight triple-bounce Bonse-Hart small-angle scattering instrument on which measurements are taken from Q= 0.0001 to 10^{-5} Å^{-1}.[17-18] All data were collected using the 3.6 Å reflection of the analyzer crystals. Raw data were reduced using the Mantid framework to calculate I(Q).[19] A background run was performed with the empty concentric cylinder geometry at the same sampling conditions. The background run was subtracted from the sample run. Neutron data were modeled using the SasView small-angle scattering software package.[20] USANS data were not normalized by intensity at Q=0, because the shape of the curve was being fitted rather than the intensity. The plotted data were reduced, unnormalized data.

$$Q = \frac{4\pi}{\lambda} \sin\left(\frac{\theta}{2}\right) \qquad \text{Eqn (1)}$$

Rheo-USANS measurements at SNS were performed using a Physica MCR501 (Anton Paar) equipped with concentric cylinder geometry and with a cap to minimize evaporation. The outer geometry was a 50 mm quartz cell, and the inner geometry was a 48 mm titanium tool. USANS rheology studies were measured at constant shear rates of either 0 Hz, 30 Hz, 200 Hz, or 500 Hz. For comparison, electrodes are generally cast at rates of 100–500 Hz for normal slot die type instruments, while casting by hand tends to be from 61 Hz to 1220 Hz based on a doctor blade with a gap of 25–500 μm. Neutron studies of uncured, 10 min cured, 30 min cured, and 60 min cured PI solution in DMF-D7 (14 wt%) and their silicon slurry counterparts.

Results and Discussion

The polyimide precursor resin binder changes color upon in-lab light (i.e., fluorescent lighting) exposure in minutes. It was hypothesized that the observed changes are a response to UV light, which would change the molecular weight and binder conformation. It was hypothesized that the observed changes are indicative of crosslinking reactions that lead to changes in PI molecular weight and conformation. To investigate these light-induced changes, PI resin was exposed to UV radiation for 0, 10, 30, and 60 min.

UV radiation induced chemical and surface changes

FTIR and GPC was performed on the PI solutions at various cure times. Figure 1 shows the FTIR spectra of the PI precursor resin after curing at various times. As stated before, PI precursors are composed of amines in the form of poly(amic acids) (Figure 1B). Amine N-H stretching peaks appear at 3352 and 3240 cm^{-1} in all FTIR spectra (Supporting Information).[4] Upon UV exposure, amides form as the feature corresponding to N-H deformation at 1553 cm^{-1} and amide C=O stretching at 1657 cm^{-1} both increase with exposure time.[21-22] Concordantly N-H

amine deformation at 1633 cm^{-1} becomes less defined further suggesting amine to amide transformation. [7, 21-22] In addition to amide formation, imide C=O stretching signal at 1779 cm^{-1} appears, which was not in the uncured PI sample, along with imide O-C-N stretching feature at 722 cm^{-1}.[7, 21-22] The GPC data shows that the molecular weight increases from 6240 to 7050 g/mol after 60 min of UV exposure (Table S1). Furthermore, the polydispersity index (PDI), which correlates with broadness of molecular weight distributions, increases from 1.08 to 1.24 with increased cure time (Table S1). While not all the amines reacted to form amide and imides, it is clear that UV radiation induces the PI crosslinking that affects the average molecular weight of the binder.
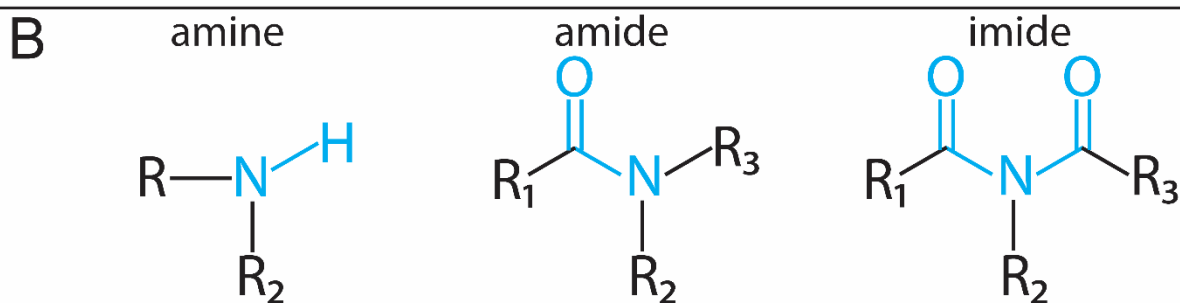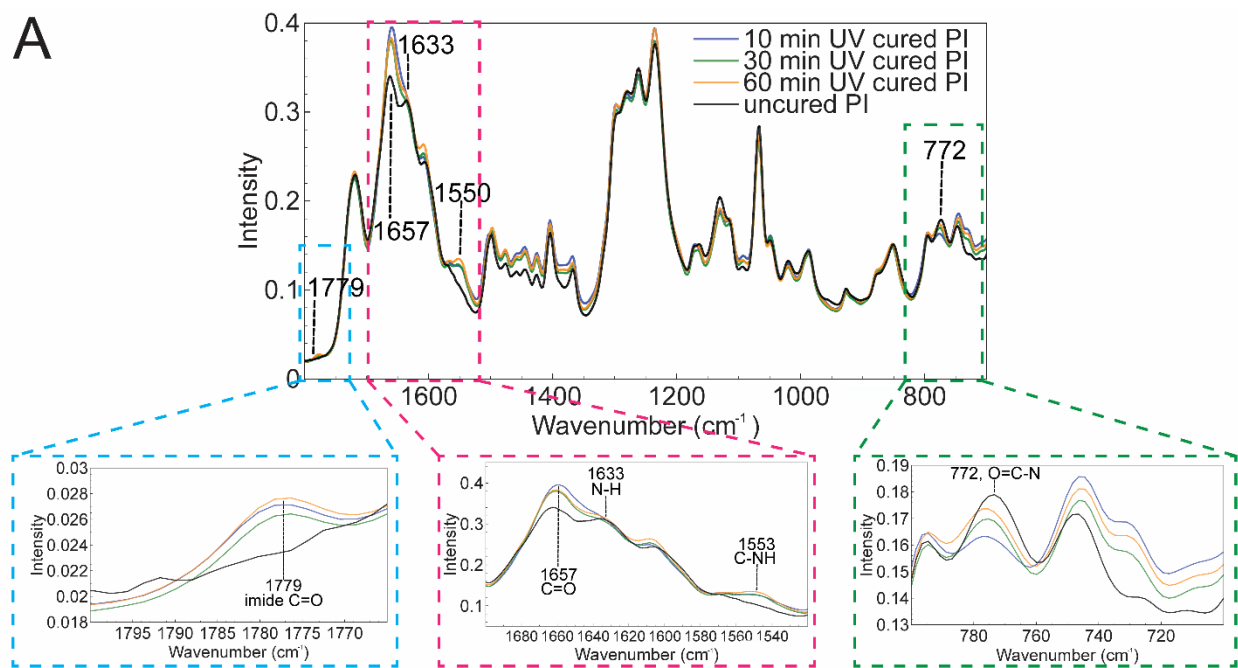
Figure 1: A) Fourier transform infrared (FTIR) spectra plotted as intensity versus wavenumber for 10 min UV cured PI solution (blue), 30 min UV cured PI solution (green), 60 min UV cured PI solution (orange), and uncured PI solution (black). The black dashed lines indicate important peaks. The blue, pink, and green dashed boxes show zoomed views of 1800-1765 cm^{-1}, 1700-1520 cm^{-1}, and 800-700 cm^{-1}, respectively. B) Structure of amine, amide, and imide functional groups where the amine groups are the most reactive and imides are the least reactive.

Rheology of PI-precursor NMP solutions as a function of aging

The light-induced changes in PI-precursor resin chemical moieties and molecular weight causes the neat PI solution rheology to change, Figure 2. Regardless of curing times, the PI mixtures with NMP are Newtonian over a wide range of shear rates (1 to 100 Hz), [23] suggesting the precursors are free flowing within this range.[24] Outside this range the mixtures shear thin, which is evident by the decrease in viscosity with shear. At low shear (< 1 Hz) the viscosity of the solutions decreases with curing time (9.1 to 7.0 Pa·s), except for the 60 min cured sample which drastically increased to 15 Pa·s, which is due to the entanglement of higher molecular weight chains. The 0, 10 and 30 min cured samples also show an isosbestic-like point at ~0.55 Hz suggesting a common agglomerate change. These measurements suggest that there are multiple microstructural changes that occur due to shear, and the extent of these changes are affected by cure time. Given that the relative ratios of amines, amides, and imides are different in each sample, it is likely that the rheological changes originates from PI self-associations being altered by changes in Van der Waals forces and hydrogen bonding.[25] An increase in hydrogen bonding seems to cause a decrease in the dispersibility as evidenced by the larger correlation length (111 to 183 nm) in the USANS data of the Si+uncured PI slurry. All of the PI solutions are Newtonian over a wide range of shear rates (0.1 to 300 Hz), [23] suggesting that the PI solutions are comprised of relatively low molecular weight species, which is corroborated by the GPC results.[24]

It was attempted to ascertain how shear rate affects the PI-precursor mixture microstructure (shape, size, and number of aggregates and agglomerates) using rheo-USANS.

However, as Figure S4 shows, the scattering intensities of all mixtures at all shear rates are low, nearing the lowest detectable limit. The mixtures were dilute (4.2 g PI-precursor in 25.8 g NMP), and the scattering contrast ($\Delta\rho$) is expected to be low, $\sim 1.311 \times 10^{-6}$ Å^{-2}. There appears to be no statistical difference between the measurements suggesting that the chemical and microstructural origin of the rheology in Figure 3 are most-likely at higher Q (smaller size domain) than detectable by USANS.
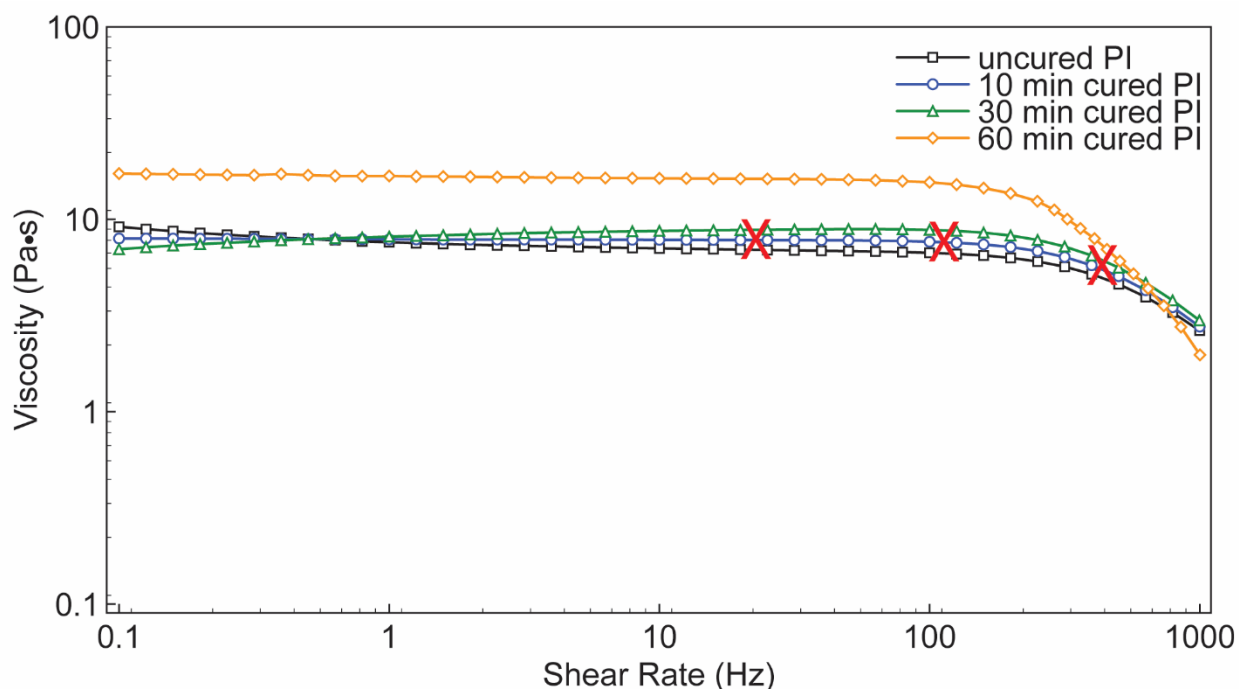
Figure 2: Viscosity versus shear rate curves of neat PI solutions with cure times of 0 min PI (i.e,. uncured, black squares), 10 min cured PI (blue circles), 30 min cured PI (green triangles), and 60 min cured PI (orange diamonds). The red X's mark the 30, 200, and 500 Hz shear rates corresponding to the shear rates at which rheo-USANS data was obtained (see Figure S4).

Structure of PI-precursor+silicon slurries

To ascertain how shear rate effects the PI-precursor mixture microstructure (shape, size, and number of aggregates and agglomerates) rheo-USANS was utilized. All scattering curves were fit with the correlation length model[26-27] (CLM, Eq. 1) to extract information on aggregate size and spacing (described in more detail in the Supporting Information section). Fitting the data with simpler models, including a simple Porod model, Guinier model, and a combination

Guinier-Porod model was attempted, but the models could not fit the data in a physically meaningful way. Therefore, the more nuanced correlation length model was chosen.[28-31]

$$I(Q) = \frac{A}{Q^n} + \frac{C}{1 + (QL)^m} + B$$

Here, A and C correspond to the number and size of agglomerates (1-10 μm) and aggregates (200 nm-1 μm), respectively. L represents cluster size (correlation length); m, cluster packing density; and n, the shape of the agglomerates. The n parameter can also represent a mass fractal where an n=1 represents elongated structures that are well solvated. As n increases to 4, the structure compacts and an n=4 represents a smooth, or hard, surface. However, to elucidate if the n value represents the shape of the aggregate or the "smoothness" of the mass fractal, a 2D detector configured for scattering at Q values less than 0.001 Å -1 is needed.[32-33] Figure 3 highlights the effect of shearing the Si+PI precursor slurries on the fitted parameters. The structure of the slurries changes as soon as the slurries are placed under shear.

There are a number of microstructural changes suggested by rheo-USANS. The parameters for aggregation (*C*) and agglomeration (*A*) increase with shear rate. Aggregates can be comprised of silicon-silicon (Si-Si) particles, silicon-PI (Si-PI) particles, or PI-PI particles. The clusters sizes (*L*) increase from ~100 nm to above 180 nm at 200 Hz. Interestingly, the cluster packing (*m* parameter, see SI) is unaffected by the UV curing time and the shear rate, remaining around 2. The general trend of agglomerate shape is also insensitive toward UV curing; agglomerates are ellipsoidal (*n* ~ 3) between 0 and 30 Hz and become spherical between 200 and 500 Hz (*n* ~ 4). The uncured slurry shows the largest resting cluster size of 111 nm (0 Hz) and the 60 min cure shows the smallest ~ 93 nm. This suggests that the number of PI chains coordinated to the particles decreases with curing time.
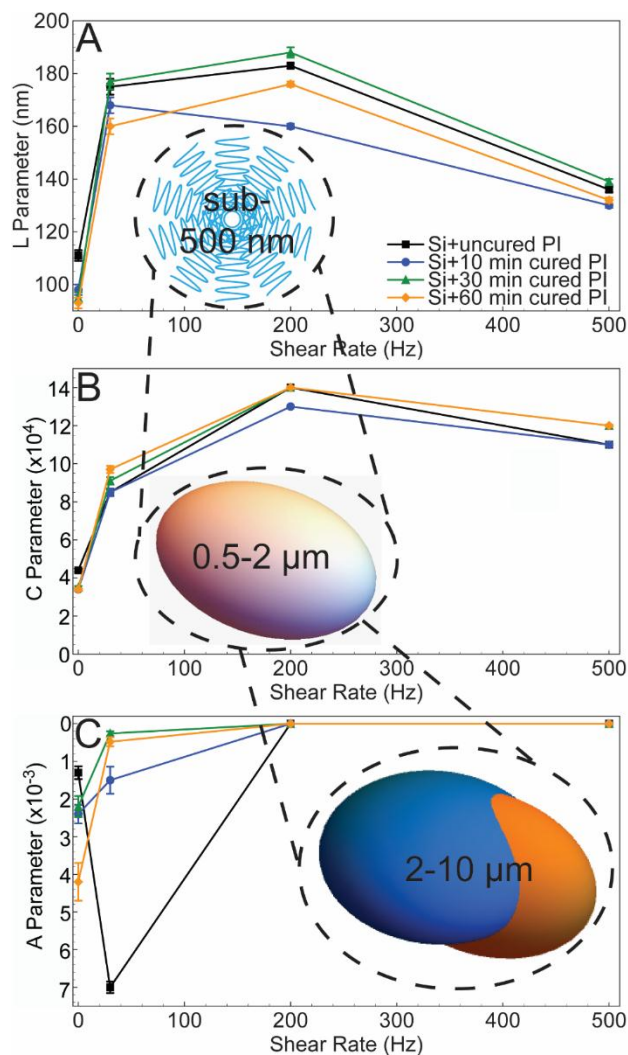
Figure 3: Graphical representation of A) values of the cluster length (L parameter), B) number of aggregates, and C) number of agglomerates as a function of shear rate for the Si+uncured PI (black squares), Si+10 min UV cured PI (blue circles), Si+30 min UV cured PI (green triangles), and Si+60 min UV cured PI (orange diamonds) slurries. Each graph has a schematic representation of the probed parameter. A cluster is a group of PI chains, Si-PI particles, or Si-Si particles and is sub-500 nm in size. Aggregates are made of two or more associated clusters and are on the order of 0.5-2 μm. Agglomerates are comprised of two or more associated aggregates and are 2-10 μm. There are error bars on all points though some are smaller than the point. Lines serve as a guide to the eye.

Figure 4 is a schematic representation of the number and size of aggregates and agglomerates. Each bounding box in Figure 4 represents the same volume, and mass is conserved in each bounding box; therefore, the flocculation or dissolution of aggregates and agglomerates are caused by either the amalgamation or desorption, respectively, of Si-Si, Si-PI, or PI-PI particles. The neutron scattering curves can be found in Supporting Information.

14

From Figure 4, it can be observed that an increase in UV cure time (i.e., aging) results in a more dispersed slurry at 0 Hz as indicated by the smaller size (by 17%) and fewer number of aggregates (by 23%) and agglomerates (by 70%) *C* and *A* parameter, See SI). The 60 min UV cured PI may be better able to keep the Si-Si or Si-PI particles from touching one another since it has longer chain lengths than the uncured PI as shown with the GPC data. From the changes in PI chemistry, the interaction between the silicon and the PI may induce differences in the aggregate and agglomerate structures.

The aggregate and agglomerate structure, as well as the cluster length of the Si+10 min UV cured PI and the Si+30 min UV cured PI are similar at 0 Hz (98 nm and 95 nm, respectively- Figures 4 and 5). The structures of the Si+10 min and Si+30 min UV cured PI fall between the curing extremes: there are a larger number of aggregates and agglomerates and a larger correlation length than the Si+60 min UV cured slurry but fewer aggregates, agglomerates, and a smaller correlation length than the Si+uncured PI slurry. There are 3 general trends in the USANS data as a function of cure time: 1) at 0 Hz, an increase in cure time results in a decrease in agglomeration, 2) at 30 Hz, the trend reverses and an increase in cure time results in an increase in agglomeration, 3) at 200 and 500 Hz, all Si+PI slurries are extremely agglomerated and have a similar number of agglomerates.
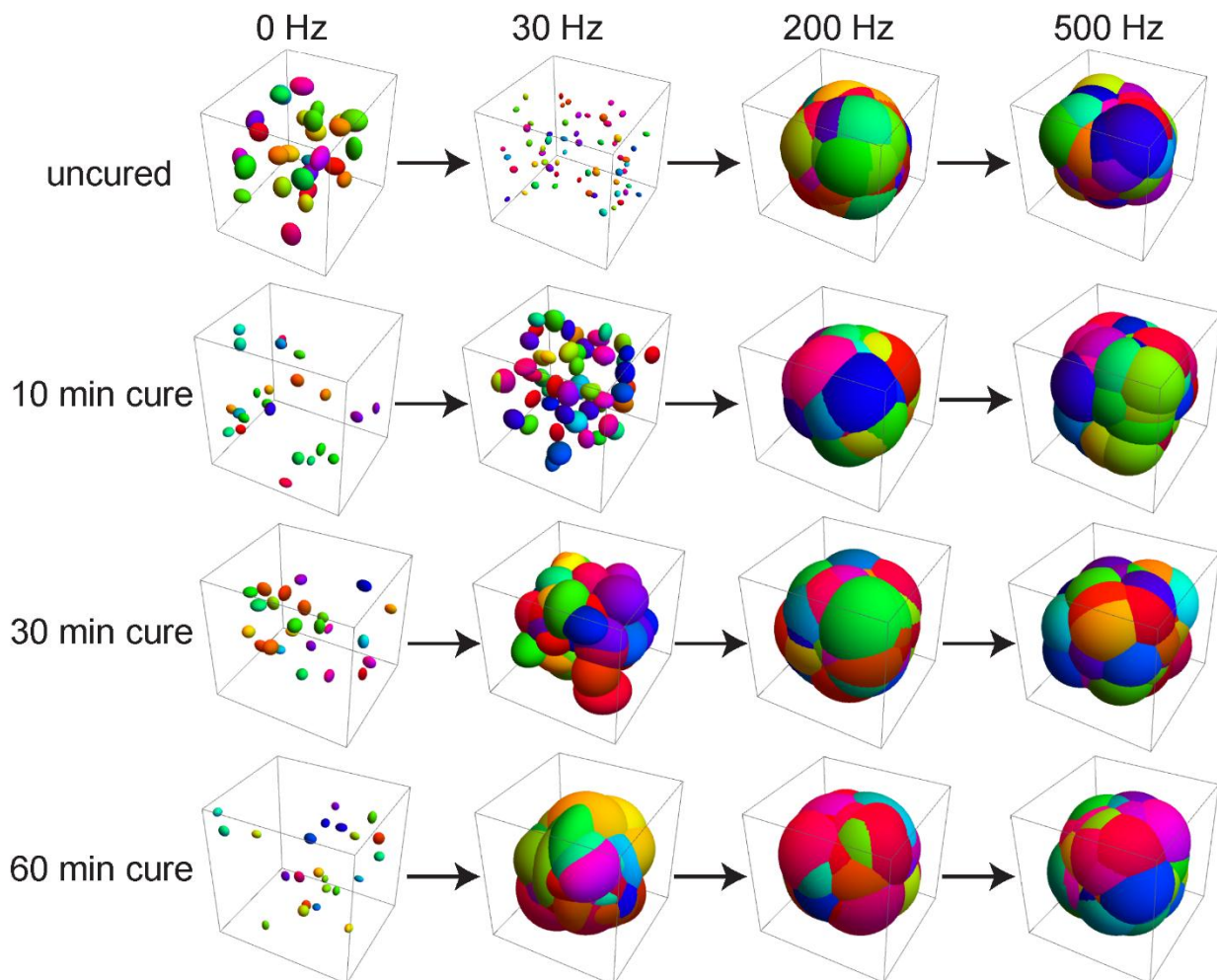
Figure 4: Schematic representation of the number and size of the aggregates and agglomerates of (from top to bottom) Si+uncured PI, Si+10 min UV cured PI, Si+30 min UV cured PI, and Si+60 min UV cured PI slurries as a function of shear rate where shear rate is (from left to right) 0 Hz, 30 Hz, 200 Hz, or 500 Hz. Each individual ellipsoid represents an aggregate and the extent of overlap represents agglomerates. The volume of each bounding box is the same.

Adding silicon particles to the PI-precursor mixture results in electrode slurries that have vastly different rheological profiles compared to the neat PI-precursor solutions, Figure 5. As expected, the viscosities of the slurries at low shear are an order of magnitude greater than their neat PI-precursor counterparts (Figure 5) due to the addition of Si and carbon black.[34] Each slurry shows two clear shear thinning regions (0.1 to 2 Hz and 6 to 1000 Hz). The viscosity plateau between 2 and 6 Hz is reminiscent of systems that show colloid dispersion phase separation.[35-37] Curing the slurry results in ~5x increase in viscosity throughout the shearing

range. This increase is likely due to the increase in crosslinking, silicon-PI bonds, and/or molecular weight.

Despite the 60 min UV cured PI having the highest molecular weight, the Si+60 min cured PI has the lowest viscosity—out of the slurries made with cured PIs—from 10 to 1000 Hz. From rheo-USANS, at 30, 200, and 500 Hz, the Si+60 min cured PI slurry has the largest number of agglomerates. Since mass is conserved in Figure 5, the Si+60 min cured PI slurry has the fewest number of sub-200 nm species as determined via rheo-USANS. Therefore, if the agglomerates do not interact with one another, the viscosity of the slurry decreases. Nevertheless, the viscosity of the Si+uncured PI electrode slurry is approximately 2x lower than that of the Si+cured PI slurries, which causes thinner electrodes with varying, uncontrolled morphologies.
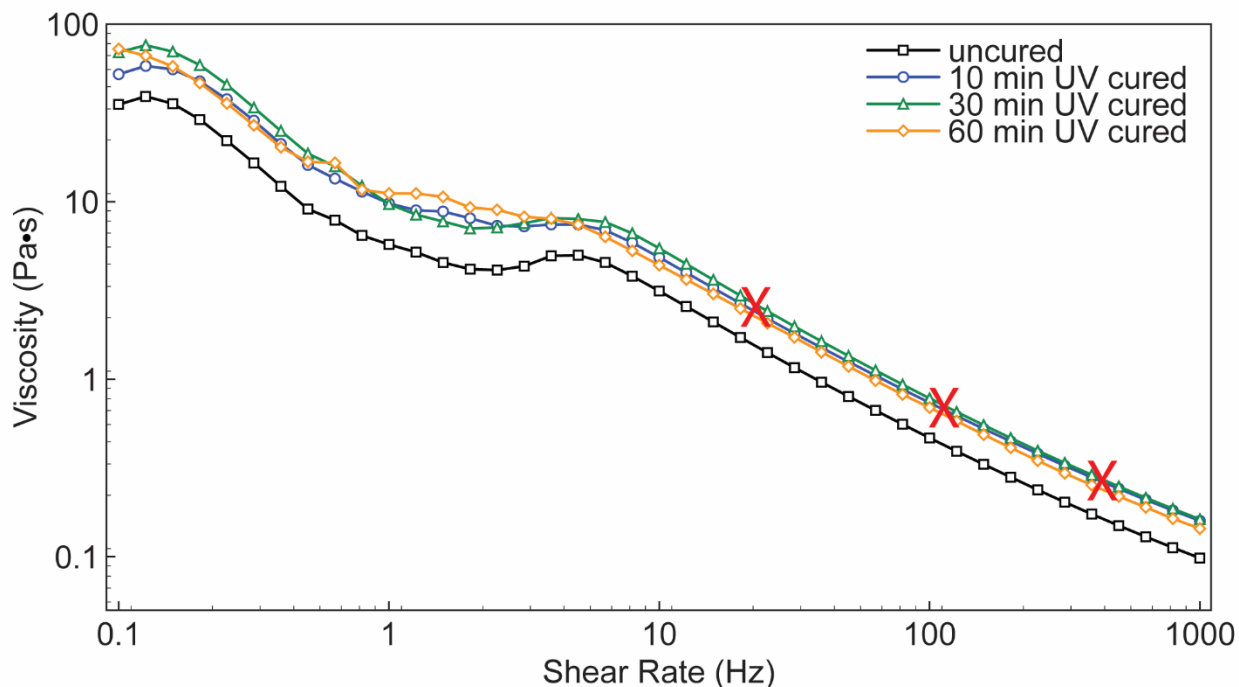
Figure 5: Viscosity versus shear rate curves of silicon electrode slurries fabricated with uncured PI (black squares), 10 min cured PI (blue circles), 30 min cured PI (green triangles), and 60 min cured PI (orange diamonds). The red X's mark the 30, 200, and 500 Hz shear rates corresponding to the shear rates at which rheo-USANS data was obtained. (Bottom)

Non-Aqueous Zeta Potential

Non-aqueous zeta potential was performed in NMP to better understand the stability of the particles and slurries at rest (Figure 6). Organic solvent-based zeta potential relies on the dielectric strength of the solvent rather than the ionic strength and pH typically used for aqueous based zeta potential. To understand the effect of each component in the electrode slurry, zeta potential of silicon, C45 carbon black, and uncured PI was obtained. The silicon particles, C45 carbon black, and uncured PI have a zeta potential of -10.6, -24.8 mV, and -10.2, respectively (Figure 6). Since a dispersion is electrostatically stable when the absolute value of the zeta potential is greater than 30 mV,[38] none of the single components are electrostatically stable in NMP. Electrostatic stabilization occurs via the balance between attractive Van der Waals forces and repulsive Coulomb forces between charged colloids (Figure 6). The combination of Si+uncured PI and Si+C45 carbon black results in an electrostatically stable dispersion with a zeta potential of -33.1 mV and -32.6 mV, respectively. Since there is an increase in the magnitude of the charge of the Si+uncured PI and the Si+C45 slurries when compared to the single components, the uncured PI electrostatically stabilizes the silicon particles, and there is an electrostatically stabilizing effect between the silicon and the C45 (Figure 6). While the zeta potential of C45+uncured PI is not statistically different from C45 alone, the refractive index data (Supporting Information) shows that there is a strong interaction between the uncured PI and the C45. Therefore, the uncured PI may be causing charge neutralization of the C45.
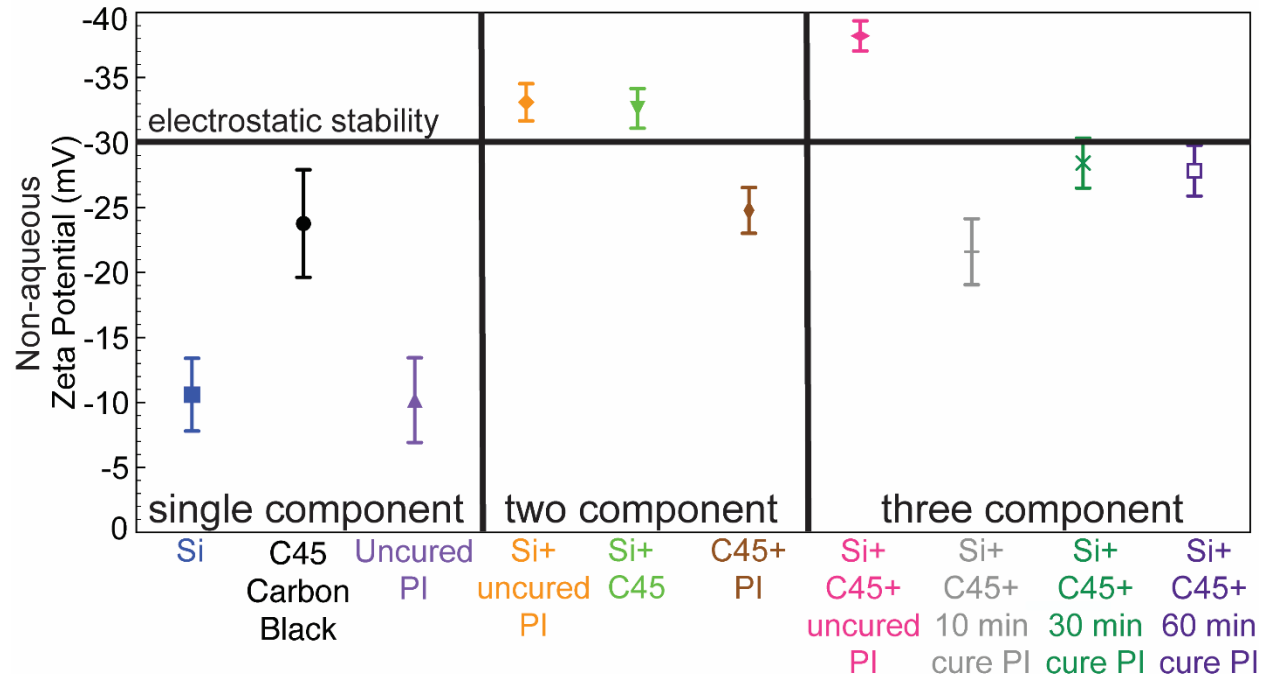
Figure 6: Single point zeta potential measurements of silicon nanoparticles (blue square), C45 carbon black (black circle), uncured PI (light purple triangle), Si+uncured PI solution (orange diamond), Si+C45 solution (light green inverted triangle), C45+uncured PI solution (brown thin diamond), Si+C45+uncured PI electrode slurry (pink horizontal diamond), Si+C45+10 min UV cured PI electrode slurry (gray plus sign), Si+C45+30 min UV cured PI electrode slurry (dark green cross), and Si+C45+60 min UV cured electrodes slurry (dark purple square). Each point is the average of 10 measurements, and error bars represent the standard error of each measurement.
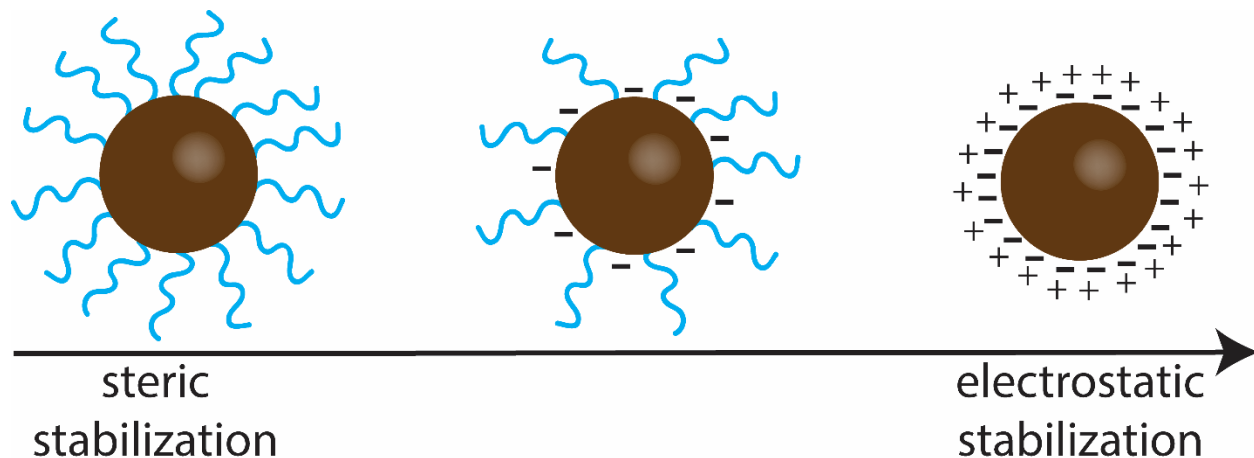
Figure 7: Schematic representation of steric stabilization (left), electrosteric stabilization (middle), and electrostatic stabilization (right).

Of the three component systems, the Si+C45+uncured PI has the highest, in magnitude, zeta potential of all the Si+C45+PI slurries (-38.1 mV). This is likely due to the combination of the electrostatic stabilization of the Si+C45 and Si+uncured PI. These three component slurries

have zeta potentials that are about a decade less than the Si+uncured PI and Si+C45 two component slurries. The Si+C45+cured PI slurries are likely sterically stabilized. Steric stabilization (Figure 7) occurs when there is an adsorbed or covalently attached polymer layer on particles that prevents their flocculation by keeping the colloids far enough away from each other so that their attractive forces do not take over. It should be noted that Figure 7 only serves as a cartoon to depict a potential steric stabilization scenario. The PI chains in the real system could look like polymer grafted nanoparticles but the polymer chains could also adsorb to the particles along their backbone. Furthermore, the Si+C45+30 min UV cured PI and Si+C45+60 min UV cured PI slurries have the same zeta potential at approximately -27 mV, while the Si+C45+10 min UV cured PI slurry has the lowest zeta potential (in magnitude) at -21.6 mV. These differences in the UV cured PI electrode slurries are likely due to the differences in chemical species present after curing discussed previously. The Si+C45+10 min UV cured electrode slurry has the three different species—imides, amides, and amines—as shown with FTIR (Figure 1), all with varying reactivities and charge stabilizations, which appear to coat the particles in a dense layer of PI, mitigating the charge on the silicon.[39-43] Additionally, there are differing dipole moments between the imide and amide functional groups, 3-4 Debye and 1 Debye,[44-45] respectively, that could cause a reduction in electrostatic (i.e., charge) stabilization. Regardless, from the USANS data at 0 Hz, the silicon slurries with UV cured PI binder are more dispersed than the silicon slurry with uncured PI binder, which suggests that steric stabilization may better disperse the system initially. This benefit is clearly lost as shear rate increases as shown in the USANS data at 30-500 Hz.

Direct Measure of Adsorption of PI on Silicon Particles

Because the USANS data suggests that PI acts as a dispersant and that 10 wt% PI seems to cause severe agglomeration of the slurry as a function of shear, it is important to know how much PI can adsorb onto the surface of the silicon. Refractive index measurements are sensitive to chemical changes. Therefore, uncured and 60 min cured PI solutions in NMP were made with known amounts of PI—from 0.25 wt% to 10 wt% PI with respect to silicon—to create a calibration curve of refractive index as a function of amount of PI in solution (Supporting Information). To see how much PI adsorbed onto silicon, solutions were made with 2 g silicon and 0.25 wt% to 10 wt% uncured PI or 60 min cured PI. After mixing, these dispersions were then centrifuged. The supernatant contained the PI that had not adsorbed onto the silicon, which can be directly measured by refractive index with comparison to the calibration curve. Figure 8 shows the mass of the PI in the supernatant, both uncured and 60 min cured PI as a function of initial PI added to the silicon slurry along with a schematic diagram of the layers on the silicon particles.

The silicon particles are only able to fully adsorb 0.25 wt% of uncured PI as shown in Figure 8. As the concentration of uncured PI in the silicon slurry is increased past 0.25 wt%, about half of the added uncured PI adsorbs onto silicon and half remains in the supernatant. It is likely that 0.25 wt% uncured PI is directly adsorbed onto the surface of the silicon, while the other uncured PI is entangled with the directly adsorbed uncured PI. When shear rate is increased, the adsorbed and entangled PI can adsorb onto more than one silicon particle, causing an increase in agglomeration.[46] This is supported by the severe agglomeration observed in the samples, especially at high shear rates.

Interestingly, 0.5 wt% of the 60 min UV cured PI can fully adsorb on the surface of the silicon particles, which is probably due to the differing functional groups present on the 60 min

cured PI versus uncured PI. The 60 min cured PI has mostly imide groups, as confirmed via FTIR, which are less likely to bind more than once to a single silicon particle or to multiple silicon particles. However, it is possible that one PI chain adsorbs onto more than one particle.[46] Indeed, the increased amount of 60 min cured PI adsorbed onto the silicon corroborates the zeta potential data which suggested that the 60 min cured PI sterically stabilizes the silicon while the uncured PI electrostatically stabilizes the silicon. However, like the uncured PI, approximately half of the 60 min cured PI remains in the sediment of the silicon slurry.
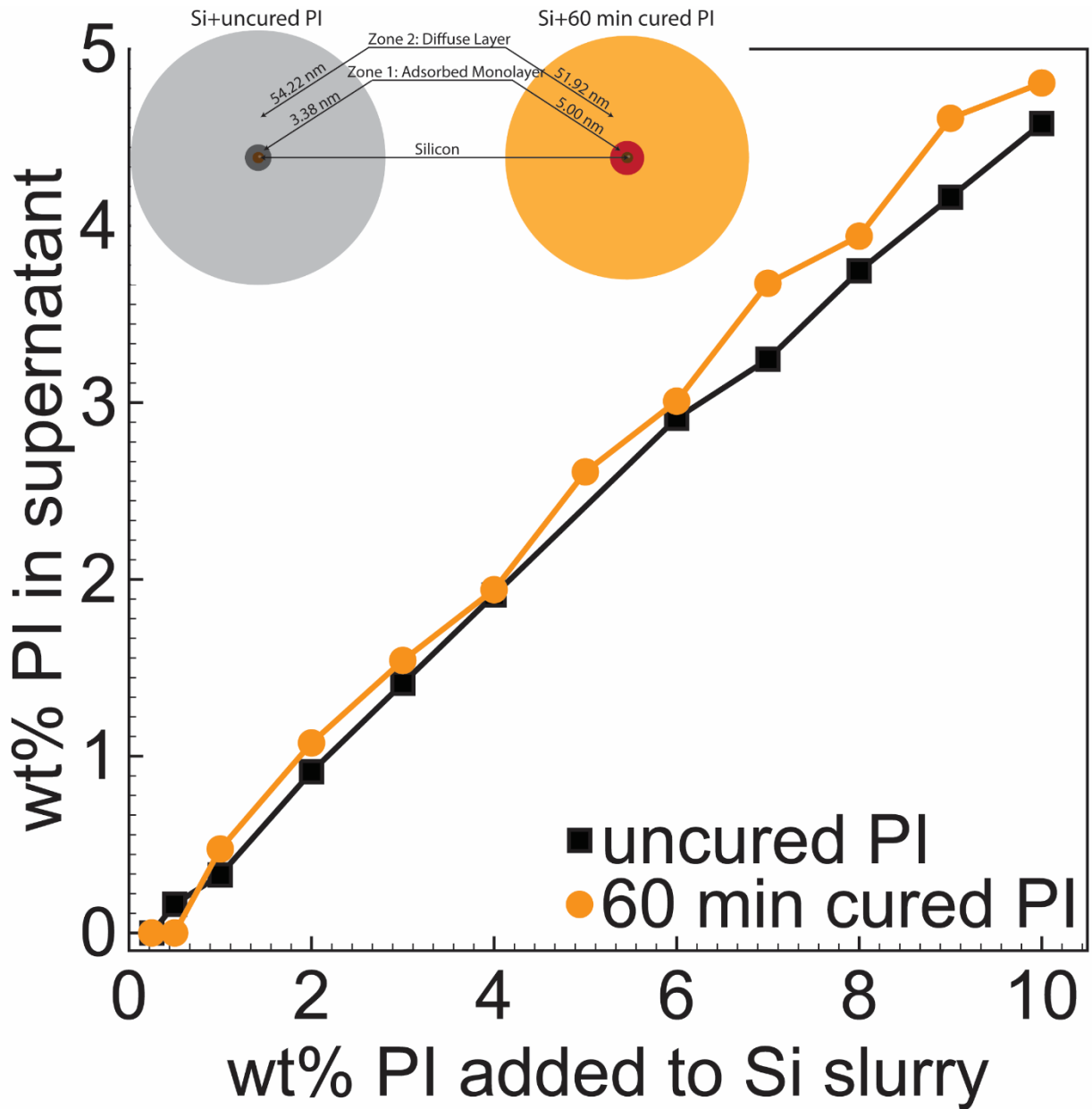
Figure 8: Amount of uncured (black squares) or 60 min UV cured PI (orange circles) in the supernatant of the silicon slurry plotted as a function of total amount of PI added to the silicon slurry. Inset: Schematic representation of the adsorption of the uncured PI (left) and 60 min cured PI (right) onto silicon. There are 2 "Adsorption Zones," where Zone 1 is the strongly bound, adsorbed monolayer (dark gray or red), and Zone 2 is the diffuse layer (light gray or yellow). The error bars are smaller than the data points. The refractive of NMP was measured as 1.4679.

Each curve in Figure 8 has 2 distinct slopes from 0-0.5 wt% and 1-10 wt%. These different slopes are similar to micropore isotherms obtained during Brunauer–Emmett–Teller (BET) measurements.[47] From the slopes in Figure 8 and the surface area of the silicon (33 m^2/g from previous BET measurements), the dimension of the adsorbed layers can be calculated. Zone

1 represents the fully adsorbed, strongly bound, PI layer on the silicon particles. For the Si+uncured PI, Zone 1 is 3.38 nm, while that of the Si+60 min cured PI is 5.00 nm (Figure 8). This shows that the 60 min cured PI more strongly associates with the silicon and may block lithium diffusion. Indeed, this may be one reason why the electrochemical performance of the Si+60 min cured PI is worse than the Si+uncured PI. Zone 2 represents the less dense, diffuse layer where the thickness of that layer is 54.22 nm and 51.92 nm for the Si+uncured PI and the Si+60 min UV cured PI slurry, respectively (Figure 8). These dimensions are similar to the correlation lengths modeled from the rheo-USANS data.

A final note about the RI data: The RI of 60 min UV cured PI is higher (1.4831 at 10 wt% PI) than that of the uncured PI (1.4798 at 10 wt%), which is indicative of both a difference in functional groups and molecular weight. A higher refractive index tends to characterize a polymer with a higher molecular weight as shown previously with other polyimide-based materials,[48-49] poly(methyl methacrylate),[50] and polystyrene.[51-52] This supports the GPC, rheology, and FTIR data that the 60 min UV cured PI has the highest molecular weight.

Electrochemical Cycling

On a commercial-type coater, battery slurries are typically cast at a wet gap between 15-50 μm depending on the needs of the electrode (i.e., specific capacity, areal loading, etc.). A wet gap of 15 μm corresponds to a shear rate of 500 Hz, while a wet gap of 45 μm is equivalent to a shear rate of 200 Hz. The 30 Hz shear rate represents the slurry being fed via gravity from the hopper to the casting area. Since the size and number of agglomerates increases substantially at 30 Hz for the Si+cured PI slurries, the slurry could be being fractionated at the hopper so the composition of the electrode may be substantially different from the expected composition.

Figure 9 presents the galvanostatic cycling curves plotted as voltage versus specific capacity for hand-cast electrodes fabricated with the various PI binders. These electrodes were hand-cast between 500 and 600 Hz, so the electrodes are in the severely agglomerated regime as shown via rheo-USANS. From the refractive index data, there are also layers of PI insulating the silicon. As such, none of the slurries lithiate/delithiate past the first cycle (Figure 9 and Supporting Information). However, in the first cycle, the Si+uncured PI electrode slurry outperforms the other electrodes (2350 mAh/g lithiation capacity versus 250-750 mAh/g). Since the agglomeration amount is similar for all Si+PI slurries at 500 Hz, the differences observed in the galvanostatic cycling of the electrodes likely arises from interactions between the silicon and the PI. From the rheo-USANS data, it seems that the uncured and 60 min cured PI binders give the best dispersion. Therefore, the mixture of amines, amides, and imides, which destabilizes the slurry as shown with zeta potential, is not beneficial in dispersing the slurry and promotes poor electrochemical properties. This may be because there is too much binder in the slurry, as shown via rheo-USANS and refractive index, which fully coats the silicon and prevents lithiation/delithiation. Nevertheless, aging the binder causes differences in slurry architecture and electrochemical performance, which can cause a problem with reproducibility of electrodes and electrochemical data.
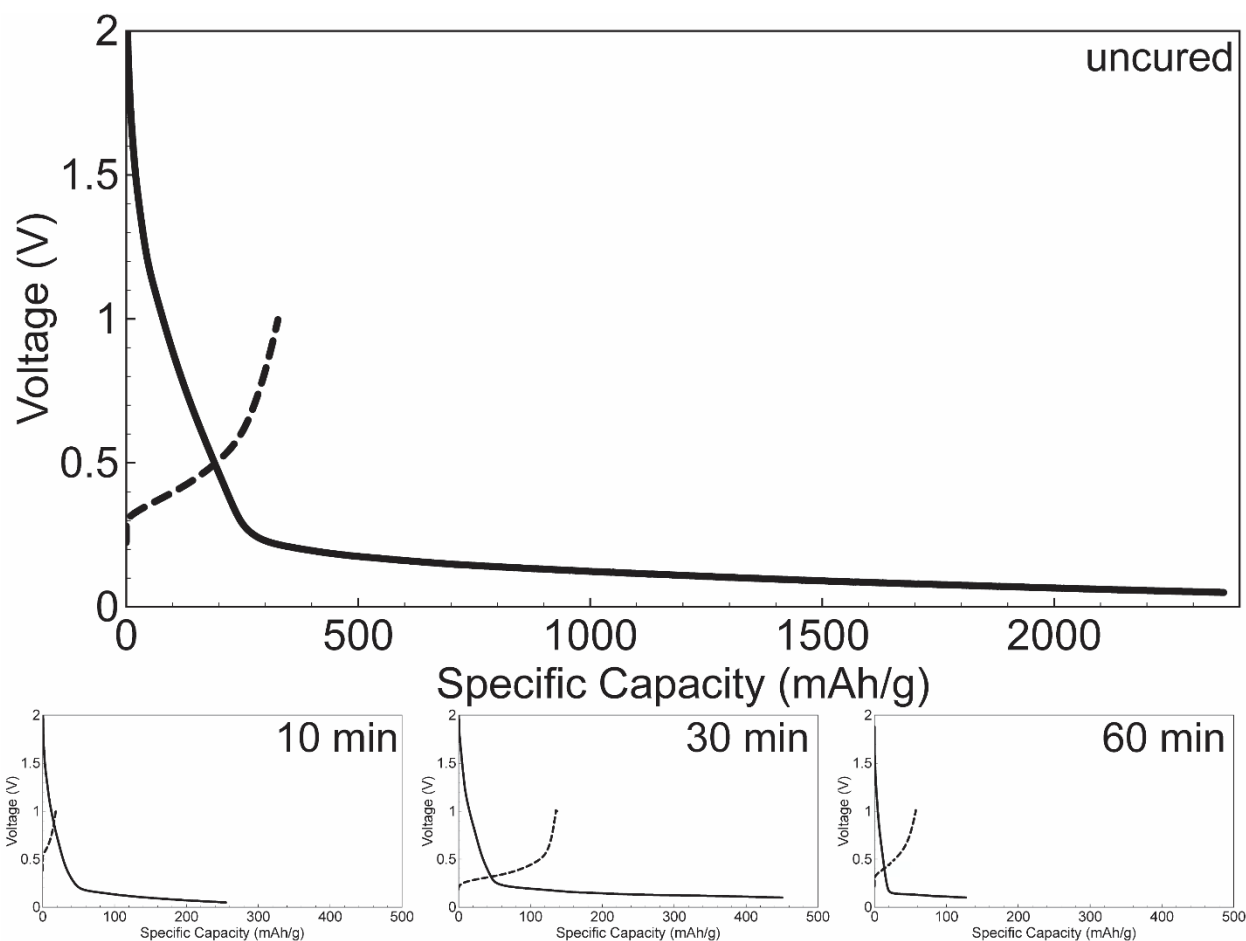
Figure 9: Galvanostatic cycling of Si+uncured PI (top), Si+10 min cured PI (bottom left), Si+30 min cured PI (bottom middle), and Si+60 min cured PI (bottom right) based electrodes plotted as voltage versus specific capacity. Notice the change of scale for the cured PI electrodes.

Comparison to other binders

It cannot go unnoticed that the cycling behavior of the Si+PI based electrodes is similar, in terms of voltage profiles, to Si/PVDF and Si/graphite/PVDF electrodes.[1, 3, 5, 9] However, PVDF based electrodes cycle past the first cycle albeit poorly. The consensus is that PVDF does not have the mechanical strength to support the volume change of the silicon produced during cycling.[53-61] However, PI based binders are known to have more mechanical strength than PVDF, but the bonding between the silicon and PI and silicon and PVDF is different. While PVDF does not bond to silicon, PI bonds to silicon through both through covalent and hydrogen bonds.[7] This

could indicate that PI covers the surface of the silicon more completely than PVDF, and prevents

lithium diffusion, as shown with the USANS data.

Binders that are generally considered "better" for silicon anodes are PAA and LiPAA. From previously obtained USANS data of Si+PAA slurries, the Si+PI slurries under shear behave in a completely opposite way to the PI in this work.[62-63] For example, as shear increases to 500 Hz, both PAA and LiPAA based silicon slurries have a 4-8 orders of magnitude decrease in the number of aggregates and agglomerates as a function of increasing shear rate. This suggests that there are much smaller species present in the PAA and LiPAA based silicon slurries at higher shear rates.

Based on GPC and previously reported viscometry data, PI—at any cure rate—has a much lower molecular weight than both PAA and LiPAA, which suggests that PI may act more like a dispersant and adsorb more readily onto the silicon particles.[64-65] From zeta potential, PI adsorbs more to silicon than PAA or LiPAA (zeta potential: approximately -40 mV).[62-63, 66] Therefore, it may be beneficial to use only a small amount of PI (less than 1 wt%) or a combination of PI as the dispersant and PAA as the binder.

The comparison of PI based slurries to PAA and LiPAA based slurries suggests that there may be an interzonal regime for the electrode architecture as schematically shown in Figure 10. In the top region, there is no binder, which causes poor cycling stability because there is nothing to support the mechanical stresses created by the lithiation/delithiation of silicon. In the bottom region of Figure 10, there is a thick, homogeneous binder coating over the silicon, which also causes poor cycling because lithium diffusion is blocked. However, there is an optimum region, or interzonal region, in the middle of Figure 10 where there is just enough binder coverage or "spotty" binder coverage on the silicon particles to support the mechanical stresses of

lithiation/delithiation and prevent electrode pulverization, but not so much binder to inhibit lithium diffusion. The current electrodes investigated are in the "homogeneous binder distribution" region, which is why they suffer from poor cyclability. To fabricate electrodes in the Interzonal Region, perhaps the precursor-based PI could be used as a dispersant and a fully cured, polymer PI could be used as the binder. Additionally, PI and PAA could be combined as the binder/dispersant system as described above. Indeed, previous work shows that adding a low molecular weight (1800 g/mol) PAA increases dispersion and lowers agglomeration resulting in electrodes with a higher initial capacity.[63] Together, this suggests that the balance between binder coverage and electrochemical properties is a careful one.
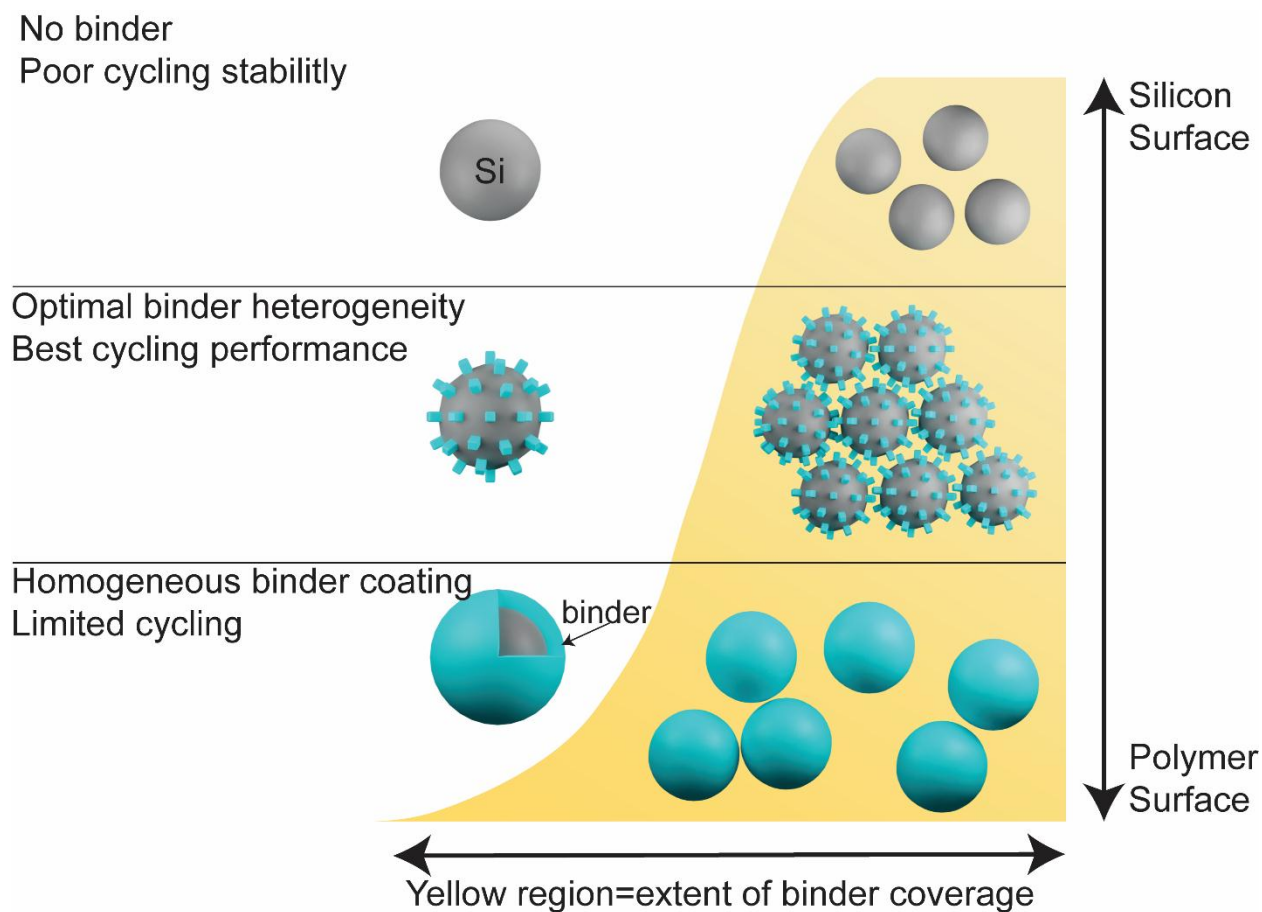
Figure 10: Schematic representation of binder coverage on silicon where the top region represents a silicon slurry with no binder in the slurry, which results in a poorly interconnected silicon anode. The bottom region represents the insulating zone where there is too much binder coverage on the silicon where lithium ions cannot diffuse to the

silicon. The interzonal region is where the silicon has "just the right amount" of binder where the binder keeps the silicon interconnected and adhered to the copper current collector but there are some bare silicon areas, which promotes lithiation.

Conclusion

Precursor-based polyimide binder is susceptible to light-induced polymerization that results in uncontrolled cross-linking and PI self-association strengths. The effect of these changes propagates onto changing the silicon slurry dynamics and electrode architectures. PI-precursor being light sensitive and its uncontrolled polymerization results in Si+PI electrode reproducibility issues. With that said, PI-precursor based slurries show severe agglomeration. Correlating changes in refractive index with precursor concentration revealed that PI precursors strongly bind with Si, leading to poor battery cycling characteristics. The shearing and binding characteristics are opposite from the observations in on Si+PAA and Si+LiPAA slurries. This leads to the conclusion that PI should be used as a dispersant with PAA/LiPAA as the binder to achieve the silicon slurry interzonal region that balances Si particle binding and networking without impeding Li insertion.

Acknowledgements

References

1.   Kim, J. S.; Choi, W.; Cho, K. Y.; Byun, D.; Lim, J.; Lee, J. K., Effect of Polyimide Binder on Electrochemical Characteristics of Surface-Modified Silicon Anode for Lithium Ion Batteries. *J. Power Sources* **2013,** *244*, 521-526.
2.   Lee, P. K.; Tahmasebi, M. H.; Tan, T.; Ran, S. J.; Boles, S. T.; Yu, D. Y. W., Polyimide Capping Layer on Improving Electrochemical Stability of Silicon Thin-Film for Li-Ion Batteries. *Mater. Today Energy* **2019,** *12*, 297-302.
3.   Hong, M. H.; Lee, S.; Choi, S.; Mun, J., Polyimide Binder for a High-Energy-Density Composite Anode Electrode with Graphite and Silicon. *J. Electroanal. Chem.* **2020,** *871*.
4.   Lee, P. K.; Tan, T.; Wang, S.; Kang, W. P.; Lee, C. S.; Yu, D. Y. W., Robust Micron-Sized Silicon Secondary Particles Anchored by Polyimide as High-Capacity, High-Stability Li-Ion Battery Anode. *ACS Appl. Mater. Interfaces* **2018,** *10* (40), 34132-34139.
5.   Oh, J.; Jin, D.; Kim, K.; Song, D.; Lee, Y. M.; Ryou, M. H., Improving the Cycling Performance of Lithium-Ion Battery Si/Graphite Anodes Using a Soluble Polyimide Binder. *ACS Omega* **2017,** *2* (11), 8438-8444.
6.   Uchida, S.; Mihashi, M.; Yamagata, M.; Ishikawa, M., Electrochemical Properties of Non-Nano-Silicon Negative Electrodes Prepared with a Polyimide Binder. *J. Power Sources* **2015,** *273*, 118-122.
7.   Yoon, T.; Chapman, N.; Nguyen, C. C.; Lucht, B. L., Electrochemical Reactivity of Polyimide and Feasibility as a Conductive Binder for Silicon Negative Electrodes. *J. Mater. Sci.* **2017,** *52* (7), 3613-3621.
8.   Choi, J.; Kim, K.; Jeong, J.; Cho, K. Y.; Ryou, M. H.; Lee, Y. M., Highly Adhesive and Soluble Copolyimide Binder: Improving the Long-Term Cycle Life of Silicon Anodes in Lithium-Ion Batteries. *ACS Appl. Mater. Interfaces* **2015,** *7* (27), 14851-14858.

9.   Choi, J.; Ryou, M. H.; Son, B.; Song, J.; Park, J. K.; Cho, K. Y.; Lee, Y. M., Improved High-Temperature Performance of Lithium-Ion Batteries Through Use of a Thermally Stable Co-Polyimide-Based Cathode Binder. *J. Power Sources* **2014,** *252*, 138-143.

10.   Fukukawa, K.; Shibasaki, Y.; Ueda, M., Direct Patterning of Poly(amic acid) and Low-Temperature Imidization Using a Photo-Base Generator. *Polym. Adv. Technol.* **2006,** *17* (2), 131-136.

11.   Herzberger, J.; Meenakshisundaram, V.; Williams, C. B.; Long, T. E., 3D Printing All-Aromatic Polyimides Using Stereolithographic 3D Printing of Polyamic Acid Salts. *ACS Macro Lett.* **2018,** *7* (4), 493-497.

12.   Hsu, S. L. C.; Wang, U.; King, J. S.; Jeng, J. L., Photosensitive Poly(amic acid)/Organoclay Nanocomposites. *Polymer* **2003,** *44* (19), 5533-5540.

13.   Ogura, T.; Higashihara, T.; Ueda, M., Direct Patterning of Poly(amic acid) and Low-Temperature Imidization Using a Crosslinker, a Photoacid Generator, and a Thermobase Generator. *J. Polym. Sci. A Polym. Chem.* **2009,** *47* (13), 3362-3369.

14.   Burdette-Trofimov, M. K.; Armstrong, B. L.; Weker, J. N.; Rogers, A. M.; Yang, G.; Self, E. C.; Armstrong, R. R.; Nanda, J.; Veith, G. M., Direct Measure of Electrode Spatial Heterogeneity: Influence of Processing Conditions on Anode Architecture and Performance. *ACS Appl. Mater. Interfaces* **2020,** *12* (50), 55954-55970.

15.   Chow, A. W.; Sinton, S. W.; Iwamiya, J. H.; Stephens, T. S., Shear-Induced Particle Migration in Couette and Parallel-Plate Viscometers-NMR Imaging and Stress Measurements. *Phys. Fluids* **1994,** *6* (8), 2561-2576.

16.   Brandl, G.; Georgii, R.; Haussler, W.; Muhlbauer, S.; Boni, P., Large Scales-Long Times: Adding High Energy Resolution to SANS. *Nucl. Instrum. Methods Phys. Res.* **2011,** *654* (1), 394-398.

17.   Carpenter, J. M.; Agamalian, M.; Iop, Aiming for the Theoretical Limit of Sensitivity of Bonse-Hart USANS Instruments. In *International Conference on Neutron Scattering 2009*, 2010; Vol. 251.

18.   Agamalian, M.; Heroux, L.; Littrell, K. C.; Carpenter, J. M.; Iop, Progress on the Time-of-Flight Ultra Small Angle Neutron Scattering Instrument at SNS. In *22nd Meeting of the International Collaboration on Advanced Neutron Sources*, 2018; Vol. 1021.

19.   Arnold, O.; Bilheux, J. C.; Borreguero, J. M.; Buts, A.; Campbell, S. I.; Chapon, L.; Doucet, M.; Draper, N.; Leal, R. F.; Gigg, M. A.; Lynch, V. E.; Markvardsen, A.; Mikkelson, D. J.; Mikkelson, R. L.; Miller, R.; Palmen, K.; Parker, P.; Passos, G.; Perring, T. G.; Peterson, P. F.; Ren, S.; Reuter, M. A.; Savici, A. T.; Taylor, J. W.; Taylor, R. J.; Tolchenoy, R.; Zhou, W.; Zikoysky, J., Mantid-Data Analysis and Visualization Package for Neutron Scattering and μSR experiments. *Nucl. Instrum. Methods Phys. Res.* **2014,** *764*, 156-166.

20.   Doucet, M.; Cho, J. H.; Alina, G.; Bakker, J.; Bouwman, W.; Butler, P.; Campbell, K.; Cooper-Benun, T.; Durniak, C.; Forster, L.; Gonzales, M.; Heenan, R.; Jackson, A.; King, S.; Kienzle, P.; Krzywon, J.; Nielsen, T.; O'Driscoll, L.; Potrzebowski, W.; Ferraz Leal, R.; Rozycko, P.; Snow, T.; Washington, A. *SasView*, 5.0; Zenodo: 2019.

21.   Pryde, C. A., FTIR Studies of Polyimides .2. Factors Affecting Quantitative Measurement. *J. Polym. Sci. A Polym. Chem.* **1993,** *31* (4), 1045-1052.

22.   Snyder, R. W.; Thomson, B.; Bartges, B.; Czerniawski, D.; Painter, P. C., FTIR Studies of Polyimides - Thermal Curing. *Macromolecules* **1989,** *22* (11), 4166-4172.

23.   Bianchi, U.; Peterlin, A., Intrinsic Viscosity of Polymers of Low Molecular Weight. *J. Polym. Sci. A-2 Polym. Chem.* **1968,** *6* (10PA), 1759-1772.

24.   Ebagninin, K. W.; Benchabane, A.; Bekkour, K., Rheological Characterization of Poly(ethylene oxide) Solutions of Different Molecular Weights. *J. Colloid Interface Sci.* **2009,** *336* (1), 360-367.

25.   Lin, X. H.; Jiang, X. Y.; Wu, W.; Mo, Y. R., Induction, Resonance, and Secondary Electrostatic Interaction on Hydrogen Bonding in the Association of Amides and Imides. *J. Org. Chem.* **2018,** *83* (21), 13446-13453.

26.   Hammouda, B., Solvation Characteristics of a Model Water-Soluble Polymer. *J. Polym. Sci. Pol. Phys.* **2006,** *44* (22), 3195-3199.

27.   Hammouda, B.; Ho, D. L.; Kline, S., Insight into Clustering in Poly(ethylene oxide) Solutions. *Macromolecules* **2004,** *37* (18), 6932-6937.

28.   Guinier, A., 30 Years of Small-Angle X-ray Scattering. *Phys. Today* **1969,** *22* (11), 25-&.

29.   Hammouda, B., Analysis of the Beaucage Model. *J. Appl. Crystallogr.* **2010,** *43*, 1474-1478.

30.   Hammouda, B., A New Guinier-Porod Model. *J. Appl. Crystallogr.* **2010,** *43*, 716-719.

31.   Feigin, L. A.; Svergun, D. I., *Structure Analysis by Small-Angle X-Ray and Neutron Scattering*. Springer: Boston, MA, 1987.

32.   Dimeo, R.; Ibberson, R.; O'Kelly, S.; Neumann, D.; Cappelletti, R.; Gehring, P., The expansion of the NIST Center for Neutron Research. *Neutron News* **2013,** *24* (1), 29-31.

33.   Van Every, E.; Deyhim, A.; Kulesza, J.; Iop, New Very Small Angle Neutron Scattering (VSANS) Instrument. In *Vi European Conference on Neutron Scattering*, 2016; Vol. 746.

34.   Cerbelaud, M.; Lestriez, B.; Ferrando, R.; Videcoq, A.; Richard-Plouet, M.; Caldes, M. T.; Guyomard, D., Numerical and Experimental Study of Suspensions Containing Carbon Blacks Used as Conductive Additives in Composite Electrodes for Lithium Batteries. *Langmuir* **2014,** *30* (10), 2660-2669.

35.   Kim, K. J.; White, J. L., Rheological Investigations of Suspensions of Talc, Calcium Carbonate, and Their Mixtures in a Polystyrene Melt. *Polym. Eng. Sci.* **1999,** *39* (11), 2189-2198.

36.   Lee, J. H.; Ruegg, M. L.; Balsara, N. P.; Zhu, Y. Q.; Gido, S. P.; Krishnamoorti, R.; Kim, M. H., Phase Behavior of Highly Immiscible Polymer Blends Stabilized by a Balanced Block Copolymer Surfactant. *Macromolecules* **2003,** *36* (17), 6537-6548.

37.   Litchfield, D. W.; Baird, D. G., The Rheology of High Aspect Ratio Nanoparticle Filled Liquids. *Rheol. Rev.* **2006**, 1-60.

38.   Bhattacharjee, S., DLS and Zeta Potential - What They are and What They are Not? *J. Control. Release* **2016,** *235*, 337-351.

39.   Hawthorne, D. G.; Hodgkin, J. H., Amine Reactivity Changes in Imide Formation from Heterocyclic Bases. *High Perform. Polym.* **1999,** *11* (3), 315-329.

40.   Lin, C. T.; Huang, T. Y.; Huang, J. J.; Wu, N. L.; Leung, M. K., Multifunctional Co-poly(amic acid): A New Binder for Si-Based Micro-Composite Anode of Lithium-Ion Battery. *J. Power Sources* **2016,** *330*, 246-252.

41.   March, J., *Advanced Organic Chemistry: Reactions, Mechanisms, and Structure*. 4 ed.; Wiley: New York, NY, 1992.

42.   Nicolaou, K. C.; Mathison, C. J. N., Synthesis of Imides, N-Acyl Vinylogous Carbamates and Ureas, and Nitriles by Oxidation of Amides and Amines with Dess-Martin Periodinane. *Angew. Chem. Int. Ed.* **2005,** *44* (37), 5992-5997.

43.   Zhang, Y.; Tan, K. L.; Liaw, B. Y.; Liaw, D. J.; Kang, E. T., Thermal Imidization of Poly(amic acid) Precursors on Glycidyl Methacrylate (GMA) Graft-Polymerized Si(100) Surface. *Thin Solid Films* **2000,** *374* (1), 70-79.

44.   Cowley, E. G., Dipole Moments of Aliphatic and Aromatic Amines. *Nature* **1951,** *168* (4277), 705-706.

45.   Lee, C. M.; Kumler, W. D., The Dipole Moment and Structure of the Imide Group. IV. Aromatic Imides: Phthalimide and Naphthalimide, Comparison of Dipole Moments of Imides and Anhydrides. *J. Org. Chem.* **1962,** *27* (6), 2055-2059.

46.   Hall, L. M.; Jayaraman, A.; Schweizer, K. S., Molecular theories of polymer nanocomposites. *Curr. Opin. Solid State Mater. Sci.* **2010,** *14* (2), 38-48.

47.   Khalfaoui, M.; Knani, S.; Hachicha, M. A.; Ben Lamine, A., New Theoretical Expressions for the Five Adsorption Type Isotherms Classified by BET Based on Statistical Physics Treatment. *J. Colloid Interface Sci.* **2003,** *263* (2), 350-356.

48.   Abe, K.; Nagao, D.; Konno, M., Fabrication of Highly Refractive $BaTiO_3$ Nanocomposite Films using Heat Resistant Polymer as Matrix. *Eur. Polym. J.* **2013,** *49* (11), 3455-3459.

49.   Li, F. M.; Kim, K. H.; Savitski, E. P.; Chen, J. C.; Harris, F. W.; Cheng, S. Z. D., Molecular Weight and Film Thickness Effects on Linear Optical Anisotropy of 6FDA-PFMB Polyimides. *Polymer* **1997,** *38* (13), 3223-3227.

50.   Cetinkaya, O.; Demirci, G.; Mergo, P., Effect of the Different Chain Transfer Agents on Molecular Weight and Optical Properties of Poly(methyl methacrylate). *Opt. Mater.* **2017,** *70*, 25-30.

51.   Itakura, M.; Sato, K.; Lusenkova, M. A.; Matsuyama, S.; Shimada, K.; Saito, T.; Kinugasa, S., Molecular Weight Dependency of Refractive Index Increment of Polystyrene Determined by Uniform Oligomers. *J. Appl. Polym. Sci.* **2004,** *94* (3), 1101-1106.

52.   Makino, K.; Akimoto, Y.; Koike, K.; Kondo, A.; Inoue, A.; Koike, Y., Low Loss and High Bandwidth Polystyrene-Based Graded Index Polymer Optical Fiber. *J. Light. Technol.* **2013,** *31* (14), 2407-2412.

53.   Hu, J. Z.; Wang, Y. K.; Li, D. W.; Cheng, Y. T., Effects of adhesion and cohesion on the electrochemical performance and durability of silicon composite electrodes. *J. Power Sources* **2018,** *397*, 223-230.

54.   Jeena, M. T.; Lee, J. I.; Kim, S. H.; Kim, C.; Kim, J. Y.; Park, S.; Ryu, J. H., Multifunctional Molecular Design as an Efficient Polymeric Binder for Silicon Anodes in Lithium-Ion Batteries. *ACS Appl. Mater. Interfaces* **2014,** *6* (20), 18001-18007.

55.   Jeong, Y. K.; Kwon, T. W.; Lee, I.; Kim, T. S.; Coskun, A.; Choi, J. W., Millipede-Inspired Structural Design Principle for High Performance Polysaccharide Binders in Silicon Anodes. *Energy Environ. Sci.* **2015,** *8* (4), 1224-1230.

56.   Liu, J.; Zhang, Q.; Zhang, T.; Li, J. T.; Huang, L.; Sun, S. G., A Robust Ion-Conductive Biopolymer as a Binder for Si Anodes of Lithium-Ion Batteries. *Adv. Funct. Mater.* **2015,** *25* (23), 3599-3605.

57.   Nguyen, C. C.; Seo, D. M.; Chandrasiri, K.; Lucht, B. L., Improved Cycling Performance of a Si Nanoparticle Anode Utilizing Citric Acid as a Surface-Modifying Agent. *Langmuir* **2017,** *33* (37), 9254-9261.

58.   Wang, Y. K.; Dang, D. Y.; Li, D. W.; Hu, J. Z.; Cheng, Y. T., Influence of polymeric binders on mechanical properties and microstructure evolution of silicon composite electrodes during electrochemical cycling. *J. Power Sources* **2019,** *425*, 170-178.

59.   Xu, J. G.; Zhang, L.; Wang, Y. K.; Chen, T.; Al-Shroofy, M.; Cheng, Y. T., Unveiling the Critical Role of Polymeric Binders for Silicon Negative Electrodes in Lithium-Ion Full Cells. *ACS Appl. Mater. Interfaces* **2017,** *9* (4), 3562-3569.

60.   Xu, J. G.; Zhang, Q. L.; Cheng, Y. T., High Capacity Silicon Electrodes with Nafion as Binders for Lithium-Ion Batteries. *J. Electrochem. Soc.* **2016,** *163* (3), A401-A405.

61.   Xu, Y. H.; Yin, G. P.; Ma, Y. L.; Zuo, P. J.; Cheng, X. Q., Simple Annealing Process for Performance Improvement of Silicon Anode Based on Polyvinylidene Fluoride Binder. *J. Power Sources* **2010,** *195* (7), 2069-2073.

62.   Burdette-Trofimov, M. K.; Armstrong, B. L.; Murphy, R., P.; Heroux, L.; Doucet, M.; Rogers, A. M.; Veith, G. M., Probing Clustering Dynamics between Silicon and PAA or LiPAA Slurries under Processing Conditions *ACS Appl. Polym. Mater.* **2021,** *3* (5), 2447–2460.

63.   Burdette-Trofimov, M. K.; Armstrong, B. L.; Murphy, R., P.; Heroux, L.; Doucet, M.; Trask, S. E.; Rogers, A. M.; Veith, G. M., Role of Low Molecular Weight Polymers on the Dynamics of Silicon Anodes During Casting. *ChemPhysChem* **2021,** *22* (11), 1049-1058.

64.   Li, C. C.; Liu, W. I.; Chen, Y. S., Efficient Dispersants for the Dispersion of Gallium Zinc Oxide Nanopowder in Aqueous Suspensions. *J. Am. Ceram. Soc.* **2017,** *100* (3), 920-928.

65.   Lasalle, A.; Guizard, C.; Deville, S.; Rossignol, F.; Carles, P., Investigating the Dispersion State of Alumina Suspensions: Contribution of Cryo-Field-Emission Gun Scanning Electron Microscopy Characterizations. *J. Am. Ceram. Soc.* **2011,** *94* (1), 245-250.

66.   Burdette-Trofimov, M. K.; Armstrong, B. L.; Rogers, A. M.; Heroux, L.; Doucet, M.; Yang, G.; Phillip, N. D.; Kidder, M. K.; Veith, G. M., Understanding Binder-Silicon Interactions During Slurry Processing. *J. Phys. Chem. C* **2020,** *124* (24), 13479-13494.